Extreme Mechanics Letters 84 (2026) 102469

Contents lists available at ScienceDirect

Extreme Mechanics Letters

journal homepage: www.elsevier.com/locate/eml

Elastic strain engineering of lattice thermal conductivity of silicon: An ab-initio study

Wencong Shi [a,b,c], Zhe Shi [a,b], Lilia M. Woods [d], Ju Li [a,b,*], Ming Dao [a,c,*]

[a] Department of Materials Science and Engineering, Massachusetts Institute of Technology, Cambridge, MA 02139, USA
[b] Department of Nuclear Science and Engineering, Massachusetts Institute of Technology, Cambridge, MA 02139, USA
[c] School of Biological Sciences, Nanyang Technological University, Singapore
[d] Department of Physics, University of South Florida, Tampa, FL 33620, USA

ARTICLE INFO

Keywords:
Strain Engineering
Lattice Thermal Conductivity
Grüneisen Parameters
Scattering Rate
Anisotropy in Thermal Conductivity

ABSTRACT

Silicon (Si) is the most essential material in the semiconductor industry. It is important to manage the thermal properties of crystalline Si. Elastic strain engineering (ESE) has proven to be an effective tool in controlling the electrical conductivity of Si in strained-silicon technology; its effects on the thermal conductivity of silicon, therefore, warrants careful investigation. The ESE effect is much more pronounced for nanostructured materials due to the ultralarge elastic strains (on the order of 10%) achievable at the nanoscale. In this work, the lattice thermal conductivity (κ_L) of Si under hydrostatic, biaxial, and uniaxial strain states is studied with ab-initio simulations, and the values of strain-dependent κ_L compare well with experimental results and existing molecular dynamics simulations. To understand the mechanisms of strain-modulated κ_L, the phonon bands, scattering rate, and Grüneisen parameters of phonon modes are computed. It is shown that strain can significantly change the anharmonicity of the crystal system, thus changing phonon scattering rates and κ_L. Our results demonstrate that ESE can reduce silicon κ_L by up to approximately 90%. Furthermore, uniaxial and biaxial strains can induce highly anisotropic thermal conductivity in Si, with relative variations up to 58.5% and 14.5%, respectively.

1. Introduction

Thermal conductivity κ is critically important across physical sciences and engineering. Fourier's foundational work established a precise definition of κ and formulated heat transfer in partial differential equations [1]. It also motivated Fourier analysis or harmonic analysis in engineering [2]. Research about κ has driven major advancements, including quantum theories of heat capacity and key industrial applications, particularly in semiconductors [3,4]. While low-κ materials are sought for thermal insulation [5], high-κ materials are essential for efficient heat dissipation in electronics [6].

Various methods exist to modulate κ, such as doping [7], introducing defects [5], or creating nanocomposites [8]. Elastic Strain Engineering (ESE) has recently been proposed as a powerful, defect-free approach [9,10]. ESE uses controlled, reversible deformation to precisely tune material properties by altering electronic structures and phonon dispersions [11–13]. The effects are especially pronounced in nanomaterials, which can sustain ultra-large elastic strains exceeding 10% [13–15].

ESE's potential for modulating thermal conductivity has been demonstrated across multiple materials. Molecular dynamics (MD) simulations show that mechanical stretching can significantly increase κ of polymers [16]. Extreme compressive strain was found to enhance κ of bulk MoS_2 [17], while biaxial tensile strain anomalously increases κ in hexagonal boron nitride due to modified phonon anharmonicity [18].

Silicon (Si) is a fundamental material in semiconductors, and strained silicon technology is a key industry milestone [19,20]. Recent advances enable achieving $> 10\%$ elastic strain in nanoscale silicon, opening new avenues for property tuning [13,15]. While previous studies focused on electronic properties, this work investigates the Si lattice thermal conductivity (κ_L) under hydrostatic, biaxial, and uniaxial strain states. In addition, the strain-state dependence and anisotropic behavior under large uniaxial and biaxial strains are explored.

2. Methods

We use the Vienna Ab initio Simulation Package (VASP) for density functional theory (DFT) calculations. The lattice thermal conductivities of Si under different elastic strains are computed via the PHONOPY and

* Corresponding authors at: Department of Materials Science and Engineering, Massachusetts Institute of Technology, Cambridge, MA 02139, USA.
E-mail addresses: liju@mit.edu (J. Li), mingdao@mit.edu (M. Dao).

https://doi.org/10.1016/j.eml.2026.102469
Received 3 September 2025; Received in revised form 9 February 2026; Accepted 3 March 2026
Available online 5 March 2026

PHONO3PY packages [21]. The strains are applied via the change of lattice parameters before proceeding to the computation of lattice thermal conductivity. In this study, the x, y, z directions are aligned with the [100], [010], and [001] crystallographic axes, respectively. A structural relaxation is performed so that the cell shape and volume can be determined. The strains simulated in the present work are chosen to stay below the known diamond-to-β-tin phase transition threshold (~11–12% compressive strain).

The full solution of lattice thermal conductivity comes from solving the Peierls-Boltzmann transport equation, and the expression for κ_L is written as [21],

$$\kappa_L = \frac{1}{NV}\sum_{qj} C_{qj}\tau_{qj}v_{qj} \otimes v_{qj}, \quad (1)$$

in which V is the volume of the unit cell, and N is the number of unit cells in the system. The subscript (q,j) stands for the phonon modes with wave vector q and polarization j, and the summation is performed over all the phonon modes in the whole first Brillouin zone. C_{qj} stands for the heat capacity for each phonon mode, $v_{qj} = \nabla_q \omega_{qj}$ stands for the group velocity of the phonon, and $v_{qj} \otimes v_{qj}$ is the dyad product of the phonon group velocity. The transport lifetime $\tau_{qj} = 1/2\Gamma_{qj}(\omega_{qj})$ is obtained from the solution of the Peierls-Boltzmann equation, with $\Gamma_{qj}(\omega_{qj})$ being the imaginary part of the phonon self-energy or phonon linewidth. The detailed expression of $\Gamma_{qj}(\omega_{qj})$ is explained in detail in [21,22].

From the above equation for κ_L, the values for C_{qj}, ω_{qj} and v_{qj} require the knowledge of phonon band information, which comes from solving the dynamical matrix of the system, and such a matrix needs the information of second-order force constants FC2. In obtaining the second-order force constant, the FC2 supercell size is set to be $4 \times 4 \times 4$, the **k**-mesh for the supercell self-consistent computation is $6 \times 6 \times 6$, and the energy cutoff for the computation is 320 eV. To fully capture the long-range effect of phonon interactions, the cutoff pair distances is not set in the full computation, although it can lead to much more expensive computational cost, the accuracy is more guaranteed. The value for the phonon lifetime $\tau_{qj} = 1/2\Gamma_{qj}(\omega_{qj})$ needs the information of third-order force constants FC3 (See equation (11) of [21]). When computing the third-order force constants using PHONO3PY, the FC3 supercell size is set to $3 \times 3 \times 3$. This size is chosen after testing the convergence of κ_L toward experimentally measured values; results confirm that a $2 \times 2 \times 2$ FC3 mesh is insufficient to obtain the correct κ_L (see Supplementary Materials, Table S1). The **k**-mesh of the FC3 supercell structure is set to $6 \times 6 \times 6$, and the energy cutoff for the computation is 320 eV. In obtaining κ_L values for strained Si, the integration mesh for the κ_L computation is set to $24 \times 24 \times 24$, and it has been tested for convergence for such a setting. The isotope scattering is not included in the κ_L computation. The GW PAW pseudo-potential of Si in VASP is chosen for the DFT computation, where the "harder" GW pseudo-potential normally gives better accuracy, due to its improved representation of short-range interatomic forces, which gives second- and third-order IFC accuracy.

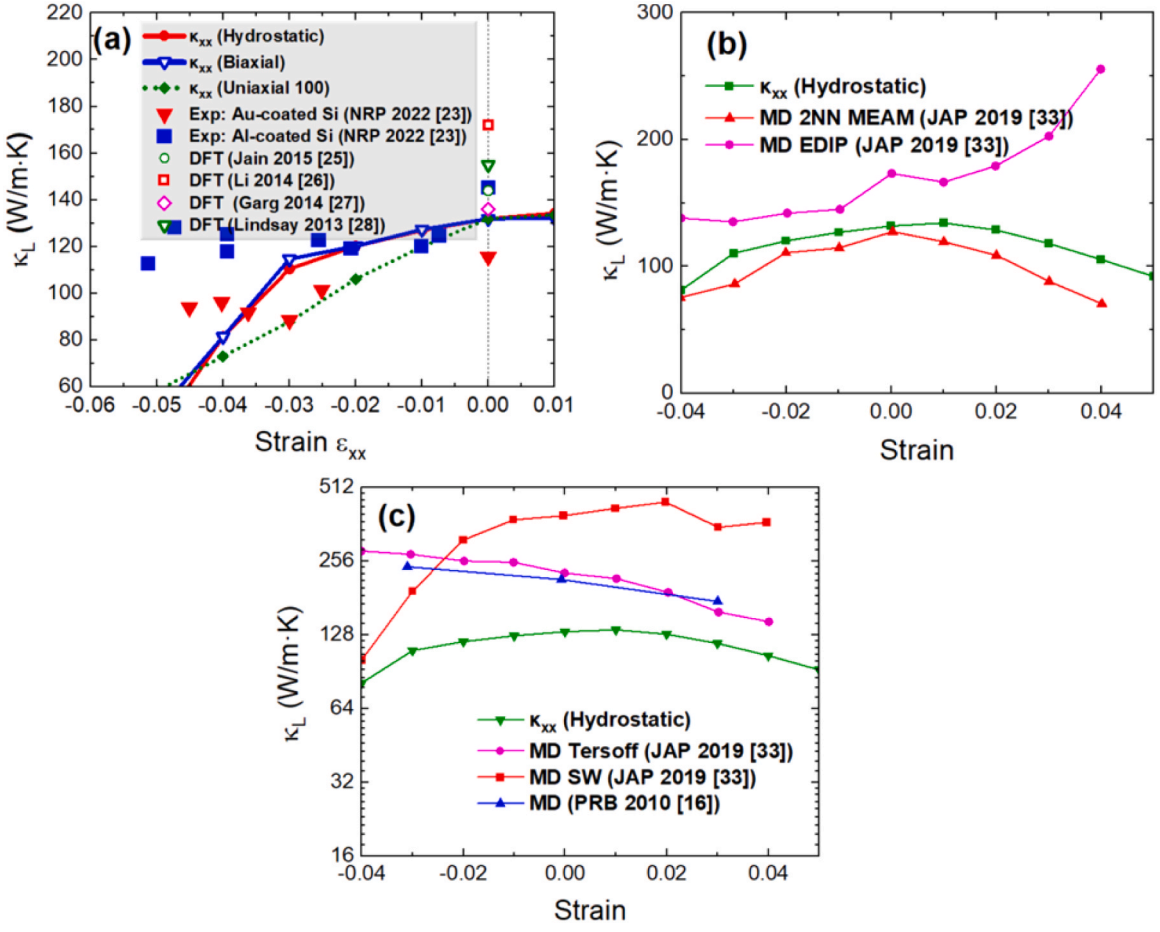

Fig. 1. (a) DFT-calculated κ_{xx} results of Si under hydrostatic strain (red solid line) and κ_{xx} under biaxial strain (blue solid line), κ_{xx} (green dotted line) under uniaxial strain (with Poisson effect neglected) in comparison with previous compression experiments, where the κ_L values at zero strain are compared with previous DFT computations. (b-c) κ_L values of Si under hydrostatic strain compared with previous MD simulations on the hydrostatic strain dependent κ_L.

3. Results

3.1. κ_L of Si compared to previous experimental and simulation results

The comparison of the computed result with existing data is shown in Fig. 1. In Fig. 1a, the scattered data points are experimental data from [23]. They show that under compressive strain, the lattice thermal conductivity of Si decreases as the magnitude of compressive stress or strain increases. Note that in [23], the measured values are stresses. Thus, here the stresses are converted into strain values for convenience, and the Young's modulus of Si is chosen to be 202 GPa as measured in [24]. Since the strain condition in the measured data is constrained in lateral directions, one needs to use the modified modulus $M = E(1-\nu)/[(1+\nu)(1-2\nu)]$, and the value is adjusted to be 247 GPa, which is a hardened value compared to the unconstrained case. To further verify the proper application of the constrained conditions, we extract the stress tensor for two representative cases: $\varepsilon_{xx} = 0.04$ and $\varepsilon_{xx} = -0.04$, with all other strain components set to zero. For tensile strain $\varepsilon_{xx} = 0.04$, the stress tensor has components $\sigma_{xx} = 6.20$ GPa, $\sigma_{yy} = \sigma_{zz} = 2.19$ GPa, and $\sigma_{xy} = \sigma_{yz} = \sigma_{zx} = 0$; whereas for compressive strain $\varepsilon_{xx} = -0.04$, the stress tensor has component $\sigma_{xx} = -6.65$ GPa, $\sigma_{yy} = \sigma_{zz} = -3.02$ GPa, and $\sigma_{xy} = \sigma_{yz} = \sigma_{zx} = 0$. This indicates that the lateral sides of the structure are not stress-free, which corresponds to the constrained conditions arising from the Poisson effect under uniaxial strain loading.

Fig. 1a also compares the κ_L values at zero strain with previous DFT computations [25–28]. The comparison shows that the result in the present work at zero strain lies between the values of the two types of Si samples in [23]. Fig. 1a shows results for hydrostatic and uniaxial strain states. The uniaxial strains are applied along the x ([100]) direction. As the experiments in [23] are performed in a way that is neither purely hydrostatic nor purely uniaxial (as there are constraints on the y and z directions), the results for hydrostatic and uniaxial loadings are all shown here. Besides, the κ_{xx} and κ_{zz} values of uniaxial strains are all shown here as the in-plane and out-plane κ values are both measured in [23], but that article did not specify which. It should also be mentioned that the experimental results for κ_L of Si under compressive strains in [23] have much higher strains than the present work's limit, shown in Fig. 1a. The reason is that the experiment can extend to the realm, where the Si structure is already changed from the diamond-cubic phase to another phase, such as the β-tin phase under high pressure, while the computation cannot capture this realm since the phonon structures are unstable.

Note that the experimental data presented in Fig. 1a are measured in Au or Al-coated Si samples [23,29], which may raise the concern of coating effects on the accuracy of thermal conductivity measurement. In fact, the measurements in Fig. 1a are performed using the well-established time-domain thermoreflectance (TDTR) method in which the measured samples are typically coated with a roughly 80 nm metal film that serves as a transducer [29–31], thus, the coating of Au or Al is an important part of the TDTR measurement. This coating plays an indispensable role as it absorbs the pump laser energy and converts it into a well-defined thermal modulation. The possible influence on the final measurement results with its introduced thermal boundary conductance might raise some concerns, but in relatively high thermal conductivity materials (>10 W/(m·K)), such as the case of Si, the influence can be neglected since the sample itself can conduct heat very efficiently.

In Fig. 1b-c, the Phono3py results are compared with some previous MD simulation values [32,33]. Fig. 1b shows data from [33] based on EDIP and 2NN MEAM potentials, which have similar trends of the thermal conductivities of Si compared with the DFT computation in this work. When under compressive hydrostatic strain, the 2NN MEAM potential in [32] has a similar trend overall compared to the present work. In Fig. 1c, the previous MD results either have a faster increasing trend of thermal conductivity under compressive strain, which does not match the experimental results in [23], or are significantly overestimated.

3.2. κ_L of Si under different strain states

Three typical cases are chosen for further studies, i.e., hydrostatic, biaxial, and uniaxial strains. The Poisson contraction effect is not taken into consideration for biaxial and uniaxial strains, as the experiments on compressive strains have lateral constraints. Fig. 2(a–c) shows the variations of κ_{xx}, κ_{yy}, and κ_{zz} under hydrostatic, biaxial, and uniaxial strains.

Under hydrostatic strain (red curves), κ_{xx}, κ_{yy}, and κ_{zz} remain identical due to symmetry. All three components decrease monotonically under compressive strain. Under tensile strain, the κ_{xx}, κ_{yy} and κ_{zz} increase slightly until $\varepsilon \approx 0.01$, then begin to decrease; however, their decline toward the tensile side is less drastic compared to that under compressive strain. Relative to their values at $\varepsilon = 0$, κ_L can increase by up to 2% and decrease by as much as 82.5% under hydrostatic strain.

Under biaxial strain (blue curves), κ_{xx} and κ_{yy} exhibit identical behavior, consistent with in-plane symmetry. Both increase steadily from $\varepsilon = -0.06$ toward zero strain, reach a peak around $\varepsilon \approx 0.01$, and then gradually decline under tensile strain. κ_{zz} follows a qualitatively similar trend but with its peak located near $\varepsilon = 0$. Compared to κ_{xx} ($= \kappa_{yy}$), κ_{zz} is mostly higher than κ_{xx} and κ_{yy} when $\varepsilon < 0$ and up to in general lower than κ_{xx} and κ_{yy} when $\varepsilon > 0$, reflecting its distinct sensitivity to out-of-plane lattice distortion. Relative to the value at $\varepsilon = 0$, κ_L can increase by up to 0.2% and decrease by as much as 87.8% under biaxial strain.

Under uniaxial strain (green curves), κ_{yy} and κ_{zz} remain identical due to the prescribed symmetry. All three components increase steadily from $\varepsilon = -0.06$ toward zero strain, peak near $\varepsilon \approx 0.01$, and then decline gradually under tensile strain. Compared to κ_{xx}, κ_{yy} ($= \kappa_{zz}$) is higher in general in the range $-0.06 < \varepsilon < 0.01$ but lower (by up to 8.1%) for $0.01 < \varepsilon < 0.06$. Relative to the value at $\varepsilon = 0$, κ_L can increase by up to 1% or decrease by as much as 87.3% under uniaxial strain.

To fully capture the changes in κ_L, the 3-phonon interactions must be considered in the full range; thus, the supercell size must go sufficiently large. This is not feasible at this time due to our limited computational resources.

To further understand the mechanisms behind the $\varepsilon - \kappa_L$ dependency, three values of $\varepsilon_{xx} = -0.04,\ 0,\ 0.04$ are picked as representative cases for hydrostatic, biaxial, and uniaxial strains. The values of κ_{xx}, κ_{yy}, κ_{zz} are tabulated in Table 1. One then studies the detailed properties of these cases to reveal the underlying reasons for the changes of κ_L values when strains are applied. In the following sections, the phonon structures, phonon linewidth (which is closely related to the phonon scattering rate), and the Grüneisen parameters are carefully studied, as they will reflect the scattering properties of the strained structures.

To elucidate the physical origin of the strain-induced anisotropy shown in Table 1, we performed a quantitative tensorial decomposition of the lattice thermal conductivity. Our analysis reveals that the anisotropy is associated with changes in both phonon group velocity and phonon lifetime along the strain axis. As illustrated in the velocity distribution histograms (Figure S1), compressive uniaxial strain ($\varepsilon_{xx} = -0.04$) induces a significant reduction in the longitudinal group velocity v_x, indicating phonon softening and bond weakening. Concurrently, the breaking of cubic symmetry O_h to D_{4h} alters the phase space for phonon-phonon scattering, preferentially enhancing scattering rates for x-polarized modes. This combined suppression of group velocity and relaxation time drastically impairs thermal transport in the x-direction relative to the transverse directions, resulting in the substantial anisotropy ratio $\frac{\kappa_{xx}}{\kappa_{zz}}$ observed in our results.

3.3. Phonon structure

Fig. 3 shows the phonon structures of Si under various elastic strains (hydrostatic, biaxial, uniaxial). Fig. 3a shows the phonon band structure

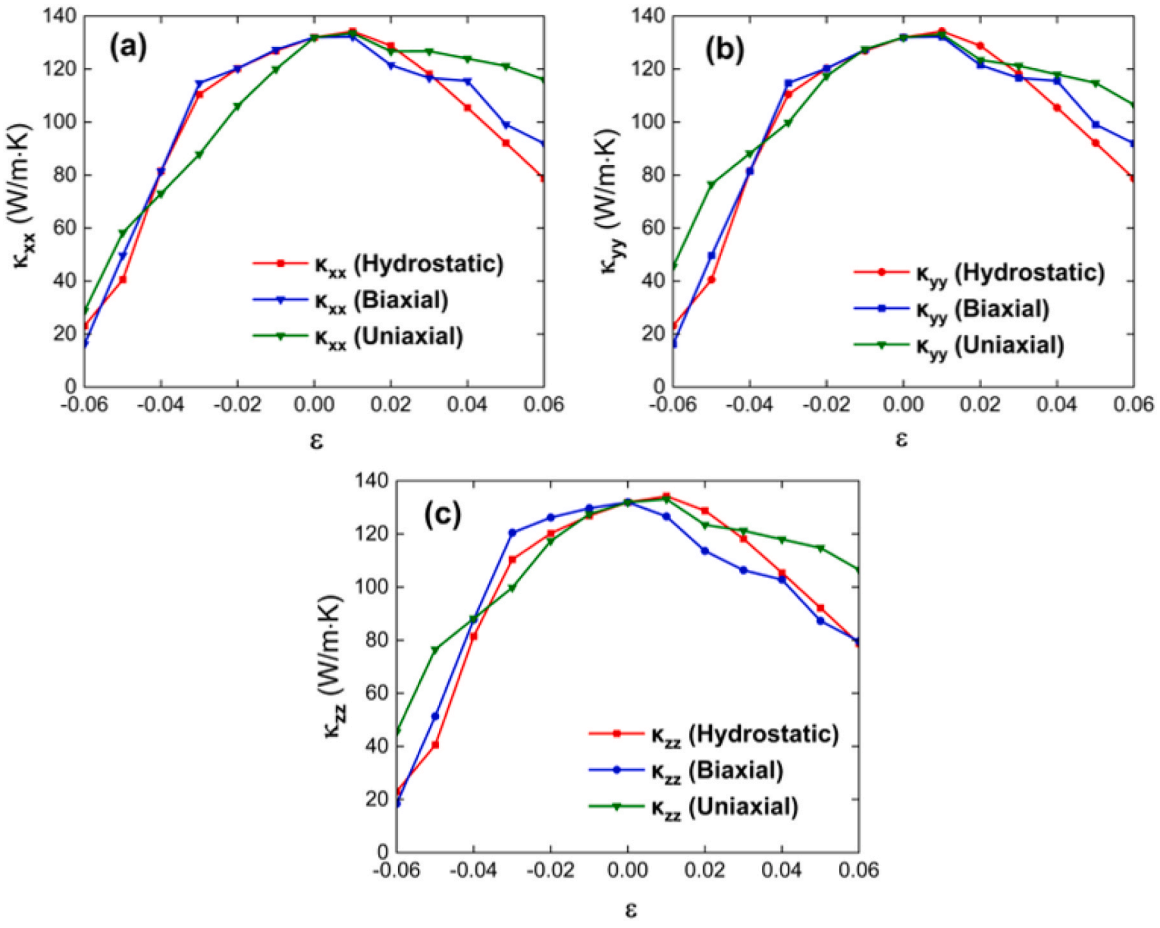

Fig. 2. κ_L values under hydrostatic, biaxial ($\varepsilon_{xx} = \varepsilon_{yy} \neq 0$, $\varepsilon_{zz} = 0$) and uniaxial ($\varepsilon_{xx} \neq 0$, $\varepsilon_{yy} = \varepsilon_{zz} = 0$) strains are compared for (a) κ_{xx}, (b) κ_{yy}, (c) κ_{zz}. The red lines are for the hydrostatic strain, the blue lines are for the biaxial strain, and the green lines are for the uniaxial strain. The maximum strain magnitudes are up to 0.06.

Table 1
κ_L component values at $\varepsilon_{xx} = -0.04,\ 0,\ 0.04$ for hydrostatic, biaxial, and uniaxial strains, in W/(m·K).

Strain	Hydrostatic			Biaxial			Uniaxial		
ε_{xx}	κ_{xx}	κ_{yy}	κ_{zz}	κ_{xx}	κ_{yy}	κ_{zz}	κ_{xx}	κ_{yy}	κ_{zz}
-0.04	81.49	81.49	81.49	81.47	81.47	87.77	73.06	88.20	88.20
0	131.9	131.9	131.9	131.9	131.9	131.9	131.9	131.9	131.9
0.04	105.4	105.4	105.4	115.5	115.5	102.8	123.9	118.0	118.0

change under hydrostatic strains. Under compressive strain $\epsilon_{xx} = -0.04$ (red dashed lines), the phonon bands for Fig. 3a-c have similar shift trends but with different magnitudes. For acoustic branches, the values are shifted to a lower position, and for optic phonon branches, the values are shifted to higher positions. For tensile strain $\epsilon_{xx} = 0.04$ (blue dashed lines), the acoustic phonon branches for Fig. 3a-c shift slightly upwards, while the optic phonon branches shift slightly downwards. Thus, all compressive strains tend to induce phonon softening on the acoustic branches, and the crystal structure has more instability. Because κ_L of Si at 300 K is governed primarily by low-frequency acoustic modes, we focus on strain-induced acoustic softening and associated scattering; shifts in optical branches are noted but are not expected to significantly impact κ_L within the present framework.

For the κ_L value, the most essential feature is the structure of the acoustic phonon branches. One thus needs to investigate the slope of these branches near the Γ point where sound velocities of the solid are determined by them. For the case of compressive strain $\varepsilon_{xx} = -0.04$, as shown in red dashed lines, the slopes near the Γ point all shift downward and most significantly for the uniaxial strain state, while hydrostatic and biaxial states show similar but smaller reductions. The observed phonon softening aligns with the reduction in κ_{xx} relative to the zero-strain value, as shown in Table 1. Under $\varepsilon_{xx} = -0.04$, κ_{xx} decreases to 81.49, 81.47, and 73.06 W/(m·K) for hydrostatic, biaxial, and uniaxial strains, respectively, with the lowest value corresponding to the strongest softening under uniaxial compression. For the case of tensile strain $\varepsilon_{xx} = 0.04$, the slopes of the acoustic branches near the Γ point (blue dashed curves) closely follow those of the zero-strain case (black curves), leading to thermal conductivity values that remain similar in magnitude for hydrostatic, biaxial, and uniaxial strain conditions.

3.4. Scattering rate

The scattering rates of the phonon are a good indication of the phonon transport lifetime. The larger scattering rates will lead to lower κ_L. The scattering rate is the inverse of the phonon lifetime and is associated with the phonon linewidth $\Gamma_{qj}(\omega_{qj})$ as $1/\tau_{qj} = 2\Gamma_{qj}(\omega_{qj})$ (see equation 146 of [34]). The PHONO3PY code can provide the information on the phonon linewidth $\Gamma_{qj}(\omega_{qj})$ of the system directly [21]. Once obtained, simply multiplication by a factor of 2 will give the

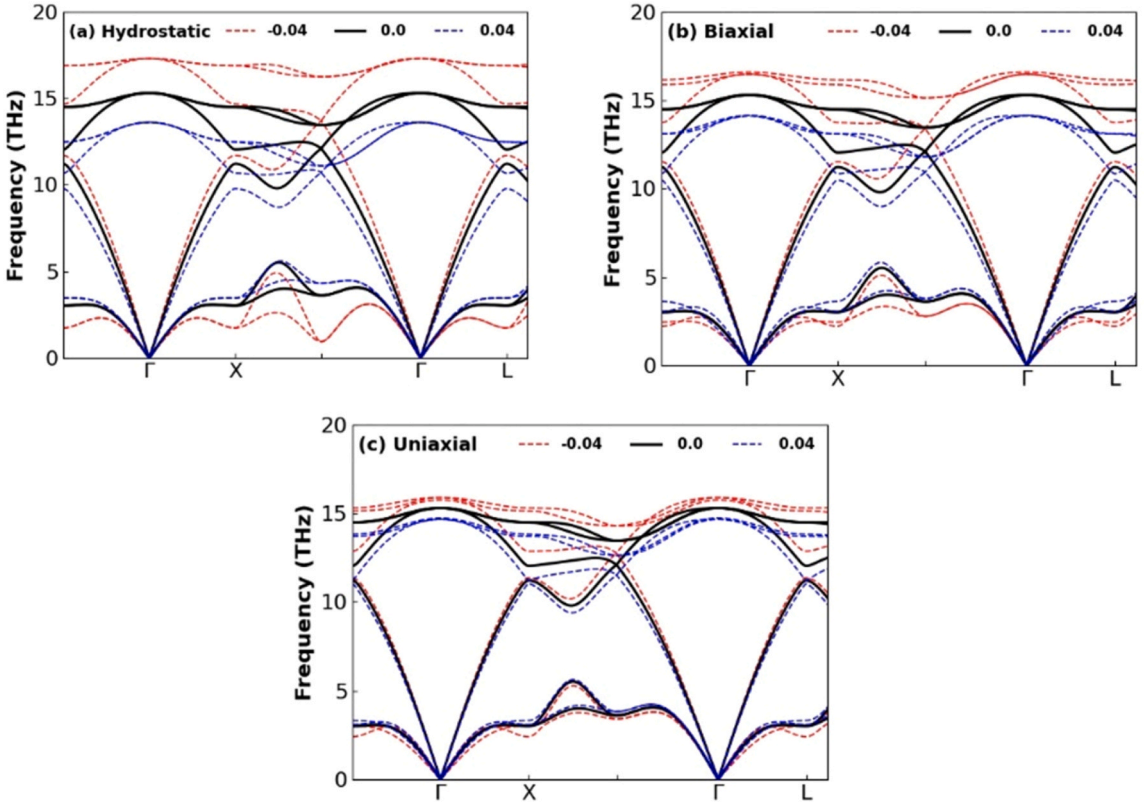

Fig. 3. Phonon bands structure for Si under (a) Hydrostatic, (b) Biaxial, (c) Uniaxial strains. The red dashed lines are for the compressive strain $\epsilon_{xx} = -0.04$, the black line is for zero strain $\epsilon_{xx} = 0.0$, and the blue dashed lines are for the tensile strain $\epsilon_{xx} = 0.04$.

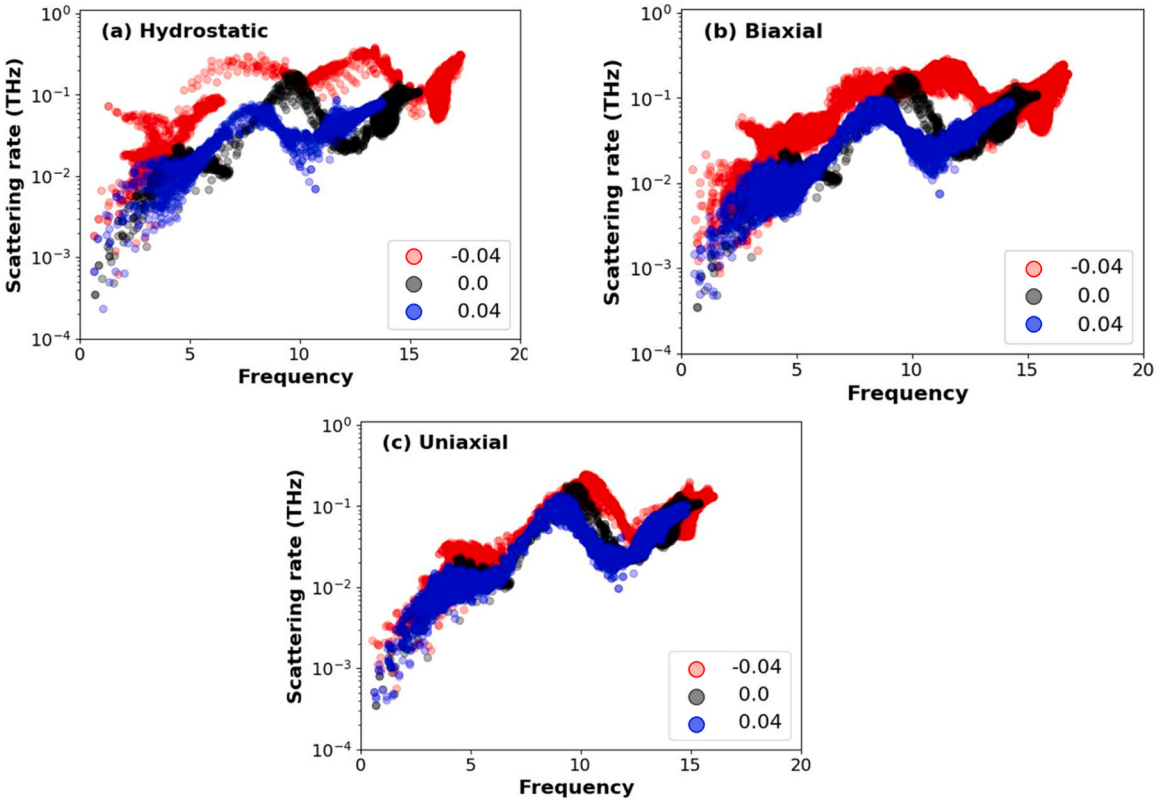

Fig. 4. Scattering rate for Si under (a) hydrostatic, (b) biaxial, and (c) uniaxial strains. Red dots represent compressive strain ($\epsilon_{xx} = -0.04$), black dots indicate the unstrained state ($\epsilon_{xx} = 0.0$), and blue dots correspond to tensile strain ($\epsilon_{xx} = 0.04$). The *y*-axis is plotted on a log scale.

information about the phonon scattering rate. Fig. 4a-c shows the scattering rates of phonon modes for three strain states. The red, black, and blue dots correspond to ε_{xx} of -0.04, 0, and 0.04, respectively.

Just as the reasoning in phonon bands discussed in the previous section, the focus of the scattering rate will be in the low-frequency range where the acoustic phonon branches are predominant. Fig. 4a-c shows dramatically elevated scattering rates for the case of compression strain $\varepsilon_{xx} = -0.04$ (as shown by red dots) at frequencies below 5 THz, compared to the zero-strain case (black dots). This pronounced increase in phonon scattering rates explains the significantly lower thermal conductivities observed under compression ($\varepsilon_{xx} = -0.04$) as shown in Table 1: 81.49, 81.47 and 73.06 W/(m·K) for hydrostatic, biaxial, and uniaxial strain, respectively, down from 131.9 W/(m·K) in the zero-strain case. For the case of tensile strain $\varepsilon_{xx} = 0.04$, Fig. 4a-c shows that the scattering rates (blue dots) largely overlap with those of the zero-strain case (black dots) at frequencies below 5 THz, with certain regions being slightly higher or lower. Such variations in scattering behavior correspond to the similarly modest reductions in thermal conductivity observed under hydrostatic, biaxial, and uniaxial tensile strains compared to the unstrained case.

Hydrostatic strain also modifies high-frequency (optical) scattering rates; while this does not alter κ_L in our analysis, it may motivate future work on how strain could influence optical/phonon-assisted responses (e.g., photoacoustic signals) once explicit photon–phonon coupling mechanisms are modeled.

3.5. Grüneisen parameters

The magnitude of the scattering rate is closely related to the anharmonicity of the structure. The third-order anharmonic coupling between interacting phonons plays a major role in determining the value of κ_L. An estimation of the value of κ_L can be written as $\kappa_L \sim \frac{M\Theta_D^3\delta}{\gamma^2 T}$, with M being the average atomic mass, Θ_D the Debye temperature, δ the atomic volume per atom, T the temperature and γ the Grüneisen parameter. Then the higher the Grüneisen parameter value, the higher the anharmonicity of the lattice and the lower the value of κ_L [35].

The Grüneisen parameter for the mode q,j is defined as $\gamma_{qj} = -\frac{V}{\omega_j(q)}\frac{\partial\omega_j(q)}{\partial V}$ with V the volume of the crystal. When the atoms are displaced within the crystal, there will be restoring forces if the force is linearly dependent upon the displacement, i.e., the forces depend harmonically on the displacements. The frequency $\omega_j(q)$ is independent of volume change. However, if the force depends nonlinearly on the atomic displacement, i.e., there are anharmonic force constants, then the frequency $\omega_j(q)$ depends on the volume change. As the κ_L values are mainly determined by the third-order phonon-phonon interaction, the strength of the Grüneisen parameters reflect the strength of anharmonicity of the crystal system: the bigger the Grüneisen parameters, the bigger the phonon-phonon scattering and the smaller the κ_L.

Results from the calculations for the Grüneisen parameters are shown in Fig. 5. As shown by the red dots in Fig. 5a–c, the absolute values of Grüneisen parameters below 5 THz increase substantially under compressive strain ($\varepsilon_{xx} = -0.04$) compared to the zero-strain case (black dots), while exhibiting clear frequency and strain-state dependence. This pronounced increase aligns with the significantly lower thermal conductivities observed under compression for all three strain states (see Table 1). The frequency-dependent and strain-state-specific modulation of anharmonicity revealed here underlies the variation in thermal conductivity across different strain states. For the case of tensile strain $\varepsilon_{xx} = 0.04$, Fig. 5a–c shows that the absolute Grüneisen parameters (blue dots) largely overlap with the zero-strain values (black dots) below 5 THz, with a slight magnitude increase in the

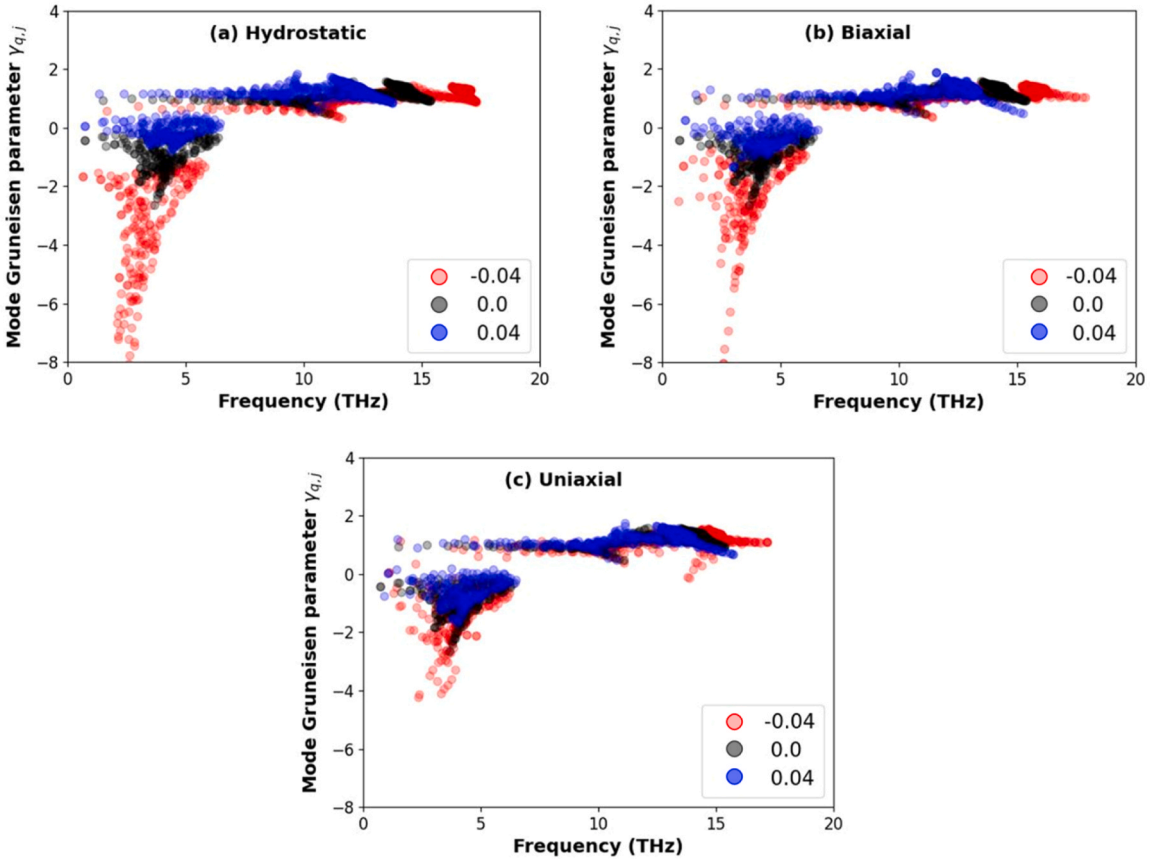

Fig. 5. Grüneisen parameters for Si under (a) hydrostatic, (b) biaxial, and (c) uniaxial strains. Red dots represent compressive strain ($\varepsilon_{xx} = -0.04$), black dots indicate the unstrained state ($\varepsilon_{xx} = 0.0$), and blue dots correspond to tensile strain ($\varepsilon_{xx} = 0.04$).

more sensitive 0–2 THz range. These modest changes in anharmonicity correspond to the similarly small reductions in thermal conductivity observed under hydrostatic, biaxial, and uniaxial tensile strains relative to the unstrained case.

4. Discussion and Concluding Remarks

The lattice thermal conductivity κ_L is a major component of thermal conductivity in insulators and semiconductors and is critically important for silicon-based devices. This study uses an ab-initio approach to compute κ_L for Si under various strains. Our results show good agreement with recent experiments under uniaxial compressive strain [23]. Our results at zero strain align more closely with experimental data than most previous DFT simulations.

For hydrostatic strain, we compare our results with those from MD simulations. Most MD potentials fail to capture the correct trend of κ_L under strain, indicating they are poorly suited for such calculations. Among the tested potentials, only the 2NN MEAM potential yields a trend similar to our ab-initio results. Others, including Tersoff, EDIP, and SW, either predict the wrong strain dependence or significantly overestimate κ_L [33].

Our results show that the $\varepsilon - \kappa_L$ dependence is different between hydrostatic, biaxial and uniaxial strain states. Thus, it's important to study the mechanisms of the strain-state dependence of κ_L. The phonon bands, scattering rate, and the Grüneisen parameters of phonons under different strain states are computed. These elastic strains significantly alter the Si phonon band structures and scattering rates, leading to changes in κ_L. Our results demonstrate that ESE can reduce silicon κ_L by approximately 90% or increase it by up to 2%. Furthermore, uniaxial and biaxial strains can induce highly anisotropic thermal conductivity in silicon, with relative variations up to 58.5% and 14.5% respectively under compressive strains.

It is worthwhile to compare the strain-induced change in thermal conductivity of silicon with that of diamond. A recent study used machine learning, trained on DFT data, to explore κ_L across 6-D strain space in diamond [11]. While tensile strains generally reduce κ_L in both materials, hydrostatic compressive strains increase κ_L in diamond but decrease κ_L in silicon (prior to any phase change). This opposing behavior under compression is also observed for uniaxial and biaxial strains. These divergent responses warrant deeper investigation and likely originate in diamond's carbon-based electronic structure, which strengthens bonds under compression. In contrast, silicon's more complex electron configuration—involving 2 s and 2p orbitals—responds differently as atomic distances decrease. This intriguing discrepancy warrants further investigation.

CRediT authorship contribution statement

Wencong Shi: Writing – review & editing, Writing – original draft, Visualization, Validation, Methodology, Investigation, Formal analysis, Data curation. **Ming Dao:** Writing – review & editing, Supervision, Methodology, Funding acquisition, Conceptualization. **Ju Li:** Writing – review & editing, Supervision, Methodology, Funding acquisition, Conceptualization. **Woods Lilia M.:** Writing – review & editing, Resources. **Zhe Shi:** Writing – review & editing, Validation, Data curation.

Declaration of Competing Interest

The authors declare no conflicts of interest.

Acknowledgments

W.S. acknowledges the support from postdoctoral fellowships from the Massachusetts Institute of Technology (USA) and Nanyang Technological University (Singapore). Z.S. and J.L. acknowledge the support from the Defense Threat Reduction Agency (USA) under Grant No. HDTRA1–20–2–0002. L.M.W. acknowledges the support from the Department of Energy (USA) under Grant No. DE-FG0206ER46297. M. D. acknowledges the support from the National Science Foundation (USA) under Grant No. DMR-2004556 and from Nanyang Technological University (Singapore) through the Visiting Professorship. We gratefully thank Prof. Subra Suresh for his guidance and suggestions.

Appendix A. Supporting information

Supplementary data associated with this article can be found in the online version at doi:10.1016/j.eml.2026.102469.

Data availability

Data will be made available on request.

References

[1] J. Fourier, The analytical theory of heat, The University Press, 1878.
[2] J.J. Benedetto, Harmonic analysis and applications, CRC Press, 2020.
[3] Y. Zhao, Y. Cai, L. Zhang, B. Li, G. Zhang, J.T. Thong, Adv. Funct. Mater. 30 (8) (2020) 1903929.
[4] O. Prakash, C.K. Dabhi, Y.S. Chauhan, H. Amrouch, Transistor self-heating: The rising challenge for semiconductor testing. 2021 IEEE 39th VLSI Test Symposium (VTS), IEEE, 2021, pp. 1–7.
[5] M. Zhao, W. Pan, C. Wan, Z. Qu, Z. Li, J. Yang, J. Eur. Ceram. Soc. 37 (1) (2017) 1–13.
[6] M. Kim, J. Kim, W. Park, J.S. Kang, Microelectron. Reliab. 170 (2025) 115782.
[7] B. Mortazavi, M. Shahrokhi, M. Raeisi, X. Zhuang, L.F.C. Pereira, T. Rabczuk, Carbon 149 (2019) 733–742.
[8] Z. Han, A. Fina, Prog. Polym. Sci. 36 (7) (2011) 914–944.
[9] S. Bhowmick, V.B. Shenoy, J. Chem. Phys. 125 (16) (2006) 164513.
[10] T. Zhu, J. Li, Prog. Mater. Sci. 55 (7) (2010) 710–757.
[11] Z. Shi, E. Tsymbalov, W. Shi, A. Barr, Q. Li, J. Li, X.-Q. Chen, M. Dao, S. Suresh, J. Li, Proc. Natl. Acad. Sci. 121 (8) (2024) e2313840121.
[12] Z. Shi, M. Dao, E. Tsymbalov, A. Shapeev, J. Li, S. Suresh, Proc. Natl. Acad. Sci. 117 (40) (2020) 24634–24639.
[13] Z. Shi, E. Tsymbalov, M. Dao, S. Suresh, A. Shapeev, J. Li, Proc. Natl. Acad. Sci. 116 (10) (2019) 4117–4122.
[14] A. Banerjee, D. Bernoulli, H. Zhang, M.-F. Yuen, J. Liu, J. Dong, F. Ding, J. Lu, M. Dao, W. Zhang, Y. Lu, S. Suresh, Science 360 (6386) (2018) 300–302.
[15] H. Zhang, J. Tersoff, S. Xu, H. Chen, Q. Zhang, K. Zhang, Y. Yang, C.-S. Lee, K.-N. Tu, J. Li, Y. Lu, Sci. Adv. 2 (8) (2016) e1501382.
[16] J. Liu, R. Yang, Phys. Rev. B 81 (17) (2010) 174122.
[17] X. Meng, T. Pandey, J. Jeong, S. Fu, J. Yang, K. Chen, A. Singh, F. He, X. Xu, J. Zhou, Phys. Rev. Lett. 122 (15) (2019) 155901.
[18] G. Qin, Z. Qin, H. Wang, M. Hu, Nano Energy 50 (2018) 425–430.
[19] M. Chu, Y.K. Sun, U. Aghoram, S.E. Thompson, Annu Rev. Mater. Res 39 (2009) 203–229.
[20] R.B. Fair, J. Appl. Phys. 50 (2) (1979) 860–868.
[21] A. Togo, L. Chaput, I. Tanaka, Phys. Rev. B 91 (9) (2015) 094306.
[22] R. Peierls, R.E. Peierls, Quantum theory of solids, Oxford University Press, 1955.
[23] Y. Zhou, Z.-Y. Dong, W.-P. Hsieh, A.F. Goncharov, X.-J. Chen, Nat. Rev. Phys. (2022) 1–17.
[24] B. Bhushan, X. Li, J. Mater. Res. 12 (1) (1997) 54–63.
[25] A. Jain, A.J. McGaughey, Comput. Mater. Sci. 110 (2015) 115–120.
[26] W. Li, J. Carrete, N.A. Katcho, N. Mingo, Comput. Phys. Commun. 185 (6) (2014) 1747–1758.
[27] J. Garg, N. Bonini, N. Marzari, First-principles determination of phonon lifetimes, mean free paths, and thermal conductivities in crystalline materials: Pure silicon and germanium. edited. Length-scale dependent phonon interactions, Springer, 2014, pp. 115–136.
[28] L. Lindsay, D. Broido, T. Reinecke, Phys. Rev. Lett. 111 (2) (2013) 025901.
[29] G.T. Hohensee, M.R. Fellinger, D.R. Trinkle, D.G. Cahill, Phys. Rev. B 91 (20) (2015) 205104.
[30] P. Jiang, X. Qian, R. Yang, J. Appl. Phys. 124 (16) (2018) 161103.
[31] D.G. Cahill, Rev. Sci. Instrum. 75 (12) (2004) 5119–5122.
[32] X. Li, K. Maute, M.L. Dunn, R. Yang, Phys. Rev. B 81 (24) (2010) 245318.
[33] V. Kuryliuk, O. Nepochatyi, P. Chantrenne, D. Lacroix, M. Isaiev, J. Appl. Phys. 126 (5) (2019) 055109.
[34] F. Giustino, Rev. Mod. Phys. 89 (1) (2017) 015003.
[35] J. Dugdale, D. MacDonald, Phys. Rev. 98 (6) (1955) 1751.